Microrheology of solutions of semiflexible biopolymer filaments using laser tweezers interferometry

Karim M. Addas,[1] Christoph F. Schmidt,[3] and Jay X. Tang[1,2]

[1]*Department of Physics, Indiana University, 727 East Third Street, Bloomington, Indiana 47405, USA*
[2]*Department of Physics, Brown University, 184 Hope Street, Providence, Rhode Island 02912, USA*
[3]*Department of Physics of Complex Systems, Vrije Universiteit, De Boelelaan 1081, 1081HV Amsterdam, The Netherlands*

Semiflexible polymers are of great biological importance in determining the mechanical properties of cells. Techniques collectively known as microrheology have recently been developed to measure the viscoelastic properties of solutions of submicroliter volumes. We employ one such technique, which uses a focused laser beam to trap a micron-sized silica bead and interferometric photodiode detection to measure passively the position fluctuations of the trapped bead with nanometer resolution and high bandwidth. The frequency-dependent complex shear modulus $G^*(f)$ can be extracted from the position fluctuations via the fluctuation-dissipation theorem and the generalized Stokes-Einstein relation. Using particle tracking microrheology, we report measurements of shear moduli of solutions of fd viruses, which are filamentous, semiflexible, and monodisperse bacteriophages, each 0.9 μm long, 7 nm in diameter, and having a persistence length of 2.2 μm. Recent theoretical treatments of semiflexible polymer dynamics provide quantitative predictions of the rheological properties of such a model system. The fd samples measured span the dilute, semidilute, and concentrated regimes. In the dilute regime $G^*(f)$ is dominated by (rigid rod) rotational relaxation, whereas the high-frequency regime reflects single-semiflexible filament dynamics consistent with the theoretical prediction. Due to the short length of fd viruses used in this study, the intermediate regime does not exhibit a well-developed plateau. A dynamic scaling analysis gives rise to a concentration scaling of $c^{1.36}$ ($r=0.99$) in the transition regime and a frequency scaling of $f^{0.63}$ ($r=0.98$) at high frequencies.

I. INTRODUCTION

Characteristic lengths that describe polymer solutions are monomer diameter d, mesh size or effective entanglement length L_e, contour length L, and persistence length L_p. L_p is the length traversed along the filament contour before the tangent vector thermally randomizes its orientation; it is proportional to the bending stiffness of the polymer. The ratio between L and L_p provides a criterion to distinguish two asymptotic classes of polymers. Flexible polymers are characterized by $L_p \ll L$, rigid-rod polymers by $L_p \gg L$. Real polymers are somewhere between the extremes, and the behavior observed depends, in general, on the length and time scales of interest. It is useful to define a third class of polymers in the intermediate regime, namely semiflexible polymers, characterized by $L_p \approx L \gg d$.

Examples of semiflexible polymers include some synthetic polymers, particularly helical polypeptides, such as poly(benzyl glutamate) (PBLG); aromatic polyamides, such as kevlar and xanthan; and a large variety of biopolymers, particularly DNA, various protein polymers, such as F-actin, microtubules and intermediate filaments, and also filamentous viruses, one of which we study in this paper. Semiflexible polymers are of great biological importance. The cytoskeletal filament F-actin, for instance, is involved in many activities, such as cell motility [1], and muscle contraction [2]. Networks of F-actin polymers, which are found preferentially in the cortex of most eukaryotic cells, also determine the mechanical properties of cells and provide a crucial link in mechanosensing biochemical networks [3]. Theoretical models for flexible [4–6] and rigid-rod [7,8] systems were developed in the late 1970s by de Gennes, Doi, Edwards, and

others. The distinctive features of single filaments as well as networks and solutions of semiflexible polymers have only recently begun to be explored, both experimentally [9–13] and theoretically [14–20]. A multitude of characteristic length scales reflected in a multitude of characteristic time scales makes, in general, for very complex behavior, even in chemically homogeneous systems. A fully quantitative understanding of the mechanics of a cell, with typically immense chemical and structural complexity, is at this time far from being reached. Progress is being made with relatively simple model systems, and the trend is to tackle increasingly complex systems.

Most polymer solutions exhibit both viscous and elastic properties. The physical quantity commonly employed to quantify the viscoelasticity of such solutions is the complex shear modulus $G^*(f)$. The most frequently used methods to measure the shear modulus involve placing the samples with volumes of order milliliters in chambers of well-defined geometry (parallel plates, cone and plate or concentric cylinders [21]). The shear modulus can be extracted from the relation between applied shear force and measured strain or vice versa.

Recently, several techniques, collectively called microrheology [11,22–25], have been developed to probe, on microscopic scales, the material properties of systems, ranging from simple polymer solutions to the interior of living cells. All the related methods use microscopic particles embedded in the sample and detect either thermal fluctuations of those particles (passive microrheology) or their response to applied forces (active microrheology). Motivations for miniaturization have been: (i) In many cases, and especially in biologi-

cal systems, only small volumes of material, typically microliters, are available. (ii) A microscopic probe offers the possibility to study inhomogeneities in the elastic properties of the polymer network on micrometer scales, for example, directly in the cytoskeleton of cells. In inhomogeneous materials, the ability to study them with probes spanning some of the characteristic microscopic length scales (e.g., approaching the interchain separation or mesh size of gels) will also lead to important new insights into the microscopic basis of the macroscopic viscoelasticity of such systems. (iii) Microrheology readily allows for measuring viscoelasticity at higher frequencies, above 1 kHz or even up to MHz, because inertia of both the probe and embedding medium can be neglected at such small length scales [26,27]. (iv) In networks of semiflexible polymers, nonlinear response occurs typically for small strains, and an advantage, particularly of using the passive technique, is that linear response parameters are measured by definition.

The microrheology method we use in this study is based on recording the thermal fluctuations of micron-sized beads embedded in the viscoelastic medium to be studied. A single probe bead is observed at a time by laser interferometry in a light microscope [11]. Detection by photodiodes ensures a bandwidth of detection between about 0.1 Hz and 100 kHz [27]. Frequency-dependent complex shear elastic and loss moduli [$G'(f)$ and $G''(f)$, respectively] are determined from the fluctuations of the embedded probes using dispersion relations from linear response theory [11].

The microrheology study is applied to a well-characterized model system of monodisperse semiflexible rods. The polymer we employ is the filamentous *E.coli* bacteriophage fd, which consists of a single-stranded circular DNA covered with a coat made of identical protein subunits [28,29]. This virus system has the advantage that particle length is extremely monodisperse (0.9 μm) [30,31]. The persistence length is 2.2 μm [32–34], and rod diameter is 7 nm. An atomic force microscopy image of virus particles adsorbed to a glass slide is shown in Fig. 1. At pH 7, the virus particles have a net negative surface charge [35], which prevents aggregation. Our experiments were performed at sufficient ionic strength (50 mM, monovalent) to largely screen electrostatic interactions [36,37]. The fd virus provides a microscopically well-controlled model system of a semiflexible polymer, which we use to test viscoelastic properties in concentration regimes spanning the dilute, semidilute, and concentrated regimes. We compare our results to theoretical predictions in the asymptotic regimes of dilute rods at low frequencies [38] and of single-filament dynamics at high frequencies [15,16]. There is currently no theoretical treatment applicable to semidilute solutions of short semiflexible polymers, and we hope to stimulate further modeling efforts by presenting our experimental results.

The rest of the paper is outlined as follows. In Sec. II we describe the methods of preparation and sample handling of the virus solutions. Section III provides an outline of the microrheology technique used, a description of the experimental setup, and data analysis methods. Experimental results and discussion will be presented in Sec. IV. Concluding remarks will be made in Sec. V. The Appendix contains a sketch of the relevant theoretical treatments of semiflexible
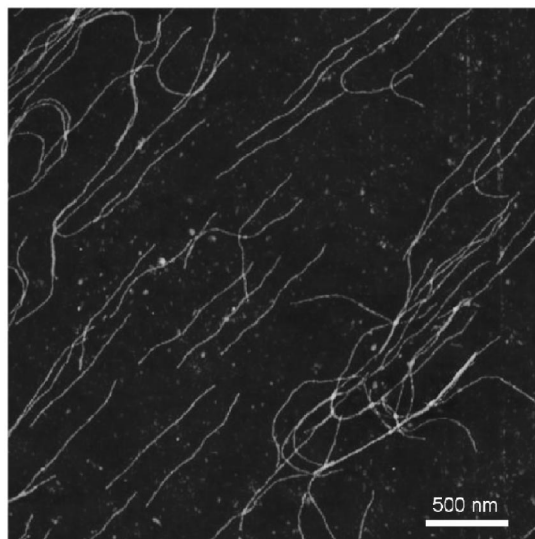

FIG. 1. AFM dry scan of fd virus filaments on a glass-slide surface. The virus has a contour length of 0.9 μm. The image was acquired using the tapping mode of a nanoscope dimension AFM.

polymer systems in the dilute, semidilute, and tightly entangled limits and a discussion of the physical mechanisms and time dependence of the different contributions to the shear modulus of such systems.

II. MATERIALS

A. Preparation of fd virus

The fd bacteriophages were prepared by a standard method [39]. Briefly, freeze-dried fd and their host E-coli bacteria (strain K38) were purchased from the American Type Culture Collection (Manassas, VA). A large amount of the progeny phages were separated from the bacterial media by multiple steps of sedimentation and resuspension, followed by a final separation step using the cesium chloride density gradient method. The virus suspensions were kept in a (5 mM imidazole, 1 mM NaN_3) buffer at pH 7.

B. Sample preparation

A concentrated stock solution of fd was prepared at 15 mg/ml, pH 7, and ionic strength I=50 mM (5 mM imidazole, 1 mM NaN_3, and 46.5 mM KCl). The concentration was determined by UV absorption at λ=269 nm (extinction coefficient ε=3.84 cm^2/mg) [31], using a Shimadzu UV 1601 Spectrophotometer. Samples for microrheology were prepared in disposable sample chambers of volume $\sim$20 μl, constructed of a microscope coverslip mounted on a microscope slide with double-stick tape ($\sim$70 μm deep). The concentrated stock solution of virus was diluted to the desired final concentration by adding a buffer solution of the same ionic composition (see above) and a solution of probe particles (silica beads, diameter 5.0 μm $<$10% standard deviation, 10% solids by mass, purchased from Bangs Laboratories, Indianapolis, IN). The beads in the final sample were diluted by $\sim$1:1000. The sample was then pipetted into the

chamber, which was sealed with vacuum grease, and then mounted onto the microscope stage.

III. MICRORHEOLOGY METHOD

A. Principle of the technique

The microrheology technique used is a passive one in which the thermal fluctuations of a micron-sized bead are used to calculate the response function of the bead by the fluctuation-dissipation theorem. The procedure outlined below is that of Schnurr *et al.* [11]. The complex single-particle response function $\alpha(f) = \alpha'(f) + i\alpha''(f)$ relates the Fourier transform $x(f)$ of the bead displacement $x(t)$ to the Fourier transform $F(f)$ of the force $F(t)$ acting on the bead

$$x(f) = \alpha(f)F(f). \tag{1}$$

The fluctuation-dissipation theorem provides the link between the single-sided Power Spectral Density (PSD)

$$S(f) = \lim_{t\to\infty} \frac{2}{t} x_t(f) x_t^*(f), \text{ where } x_t(f) = \int_{-t/2}^{t/2} x(t') e^{2\pi i f t'} dt' \tag{2}$$

and the imaginary part of the response function by

$$\alpha''(f) = \frac{\pi}{2k_b T} f S(f), \tag{3}$$

where k_b is the Boltzmann constant, and T is the solution temperature.

A Kramers-Kronig relation can then be used to calculate the real part of the response function, provided that $\alpha''(f)$ is known over a large enough frequency range [11]

$$\alpha'(f) = 4 \int_0^\infty dt \cos(2\pi f\, t) \int_0^\infty d\xi \alpha''(\xi) \sin(2\pi\xi\, t). \tag{4}$$

The connection between the response of the bead and the complex shear modulus $G(f) = G'(f) + iG''(f)$ of the viscoelastic medium surrounding the bead is assumed to be provided by the generalized Stokes-Einstein relation (GSER) [11]

$$G(f) = \frac{1}{6\pi a\ \alpha(f)}, \tag{5}$$

where G' and G'' are the elastic and loss moduli respectively, and a is the radius of the bead. This expression reduces to the familiar result for a spherical probe particle in a purely viscous medium of viscosity η, $G(f) = -i2\pi f\eta$. The GSER does not take into account the possibility of the probe particle coupling to modes of the system other than shear modes, i.e., compressional modes, or the importance of inertial effects of the particle and medium at high frequencies. The validity of the GSER in a viscoelastic two-fluid medium model in the continuum limit has been addressed by Levine and Lubensky [26]. The GSER was found to be a good approximation to the full-response function in this model within a certain frequency regime. Traditional rheology operates at much lower frequencies and by design directly excites shear modes, thus avoiding these complications.

B. Experimental setup

Microrheology was performed in a custom-built light microscope using a focused laser beam and laser interferometry to optically trap the probe particle and to record the thermal motions of individual probe particles as described in detail previously [11,40]. To detect motions of beads imbedded in the gel we used an interferometer [40] with near-infrared laser illumination (1064 nm cw, Topaz 106c, Spectra Physics, Mountain View, CA). The laser beam passes through an optical isolator, which prevents back reflections into the laser, then through a beam expander, which increases the efficiency of optical trapping. A combination of half wave plate and polarizer control the power of the beam, and two lenses in a telescope configuration allow control of the position of the beam focus in the plane perpendicular to the beam direction. The beam enters the microscope after reflection off a dichroic mirror and is brought to a focus in the sample chamber by a high NA objective (100× NA 1.3, Neofluar, Zeiss, Jena, GmbH). The laser light emerging from the condenser lens, after passing through the sample, is projected onto a quadrant photodiode in such a way that the back focal plane of the condenser is imaged [40]. An outline of the setup is presented in Fig. 2(a), and a sketch of the sample chamber and detection scheme is presented in Fig. 2(b). The signals from the four quadrants of the photodiode are combined to obtain X and Y voltages corresponding to the displacements of the bead in these directions in the plane normal to the propagation direction of the laser. The output voltages are, after analog amplification and preprocessing, recorded using an A–D interface (200 kHz, ChicoPlus, Innovative Integration, Simi Valley, CA) and data acquisition software written in Labview (National Instruments, Austin, TX). All experiments reported here were performed at two sampling rates, 20 kHz and 195 kHz (antialias filtered at about 10 kHz and 100 kHz, respectively). High bandwidth of detection was made possible by using a special-purpose fully depleted *p*-type silicon photodiode [YAG444-4A, Perkin Elmer, Vaudreuil, Canada (denoted Si-HB)] [27]. This diode was designed for fast detection of 1064 nm light and was operated at a 100 V reverse-bias voltage. Position data for each bead was normally recorded until two million data points were acquired per channel. Autocorrelations and Kramers-Kronig integrals were performed using software developed in the lab, written in C++. The resulting response data were analyzed with Mathematica 4.2 (Wolfram Research, Champaign, IL) to obtain the shear moduli.

After loading a sample, the optical trap was used to position the 5 μm diameter beads about 30 μm above the bottom surface of the chamber to minimize the surface boundary effect. The influence of the surface effect was tested at a number of distances from the microscope slides, and at larger than 20 μm, the obtained G' and G'' values were found to vary less than 5% and thus the error was deemed negligible (data not shown).

C. Calibration

Position data were recorded at different laser powers ranging from 6 to 200 mW, measured just before the beam
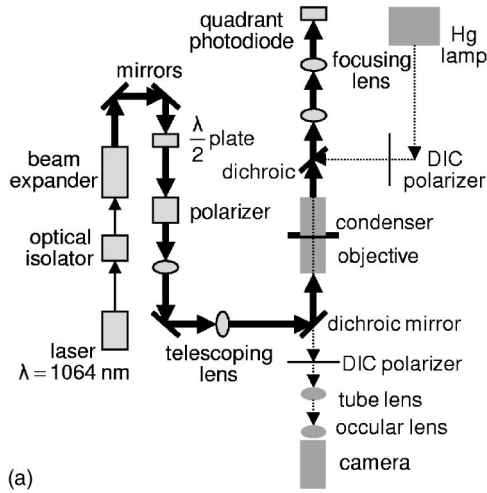
(a)
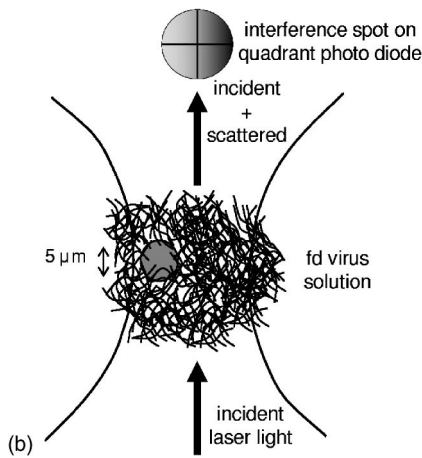
(b)

FIG. 2. (a) An outline of the essential components of the laser and optical paths. (b) Sketch of an fd sample with a bead in a laser trap and a quadrant photo diode, which detects the position of the bead.

(a)

(b)

FIG. 3. (a) PSD of nine different beads in buffer. The values are calculated from X and Y voltage data for each bead. The dotted line indicates the frequency above which the signal is strongly attenuated by an anti-aliasing filter. Inset: X (closed circles) and Y (open circles) calibration factors for each of the nine beads obtained from their respective power spectra. The straight lines show the averaged calibration factors over the nine beads for X (solid) and Y (dashed) directions. (b) The X and Y power spectra of (a) averaged over all beads.
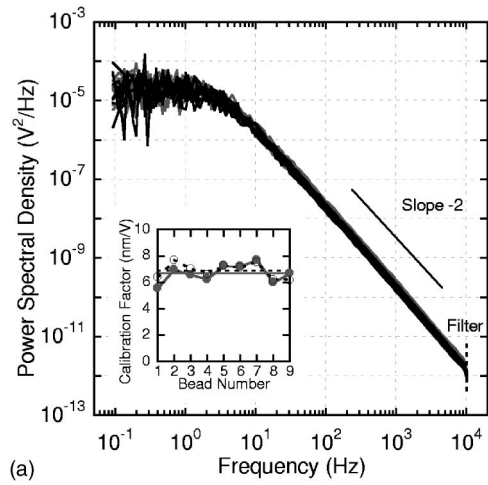
enters the microscope optics. The actual power in the specimen is about a factor of 2 lower, depending somewhat on beam diameter. The calibration factor R for each power and direction relates the quadrant diode output voltage to the actual position of the trapped bead with respect to the trap center. The calibration factor is obtained by observing the thermal fluctuations of beads in buffer solution taken at the same power settings as for the actual samples of interest [41]. The PSD of a bead in buffer has a Lorentzian form
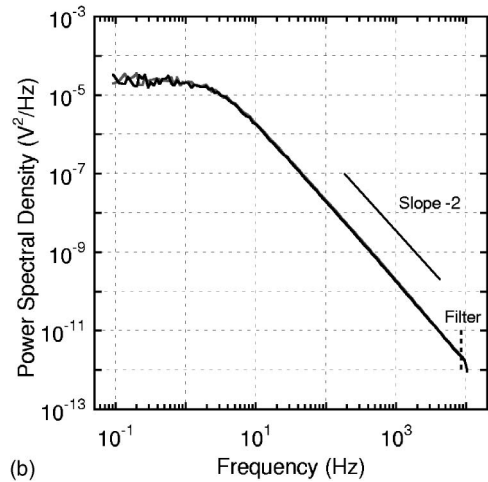
$$S(f) = \frac{S_0 f_c^2}{f_c^2 + f^2}, \qquad (6)$$

where S_0 is the low-frequency plateau value, and f_c is the corner frequency. The calibration factor is [42]

$$R(m/V) = \sqrt{\frac{k_b T}{6\pi^3 \eta a S_0 f_c^2}}. \qquad (7)$$

In the limit of high frequency, but before solvent inertial effects become significant, $S_0 f_c^2 = S f^2$ and so the high-frequency points of $S f^2$ can be used in Eq. (7) to obtain the

calibration factor (method one). One could also use a form of the PSD (which includes solvent inertial effects [27,43]), fit the data to it, and extract $S_0 f_c^2$ from the fit (method two). Both methods were compared and calibration factors were found to agree within 5%. PSD data for one power setting, before applying calibration factors, taken for nine different beads in buffer are shown in Fig. 3(a). The calibration factors extracted from these PSDs are shown for the nine beads in the inset along with the average value for each direction. These average values were used to convert diode voltage values into position data. From the spread in the X- and Y-calibration factors, we estimate a polydispersity in bead size of 9.3% standard deviation. The PSDs for motion in the X- and Y-directions, respectively, averaged over all beads are presented in Fig. 3(b).

Averaged PSDs (over nine beads and both directions) are shown in Fig. 4 along with their calibration factors (inset) for
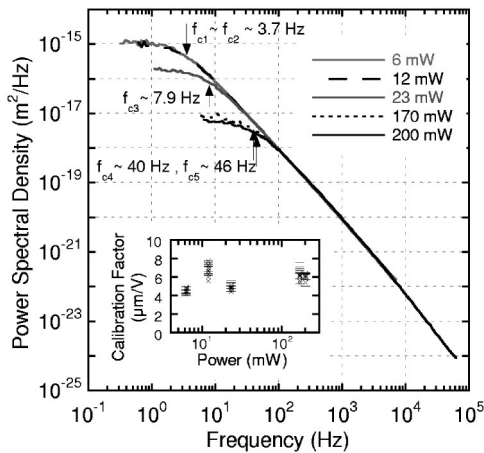
FIG. 4. PSD averaged over several beads in buffer for five different laser powers. The corner frequency for each power is indicated with an arrow. Inset: Calibration factors of all beads for X (crosses) and Y (dashes) directions for each of the five laser powers.

five different power settings. The corner frequencies for each power are indicated with arrows, and are seen to increase with power as expected, whereas the low-frequency plateau values are seen to decrease with increasing power, again as expected [41].

We used Eqs. (3)–(5) to calculate the shear loss modulus from the buffer PSDs for a 5 μm diameter bead. The loss moduli measured at two sampling rates (20 kHz and 195 kHz) are plotted in Fig. 5 (filled symbols). The data agree well with the expected straight line based on the Stokes drag loss modulus relation $G'' = 2\pi\eta f$ (dashed line). The viscosity of water η was 0.969×10^{-3} Pa·sec at the measured room temperature of 21.4 °C. The G'' data points

are higher than the straight-line Stokes relation at frequencies above 5 kHz (indicated by an arrow in Fig. 5). The reason for this is that solvent inertia can no longer be neglected at such high frequencies [27,43].

D. Trap correction

A simple viscous fluid, such as the watery buffer, has no elastic modulus, but on computing $G'(f)$ from the buffer PSD data, we find frequency independent G' values varying with the trapping laser power (Fig. 5). These observed apparent moduli are due to the harmonic confinement of the beads by the laser trap. In a viscoelastic sample, such as the fd solutions, this trap-generated modulus adds to the actual elastic modulus of the sample while it does not influence the viscous modulus. In order to obtain the true fd elastic modulus, the trap stiffness κ must be corrected for. The relationship between the response function $\alpha_{true}(f)$, which reflects the elastic confinement by the polymer network, not including the trap effect, and the measured complex response $\alpha_{measured}$ is [44]

$$\alpha_{true} = \frac{\alpha_{measured}}{1 - \kappa\alpha_{measured}}, \tag{8}$$

which upon inversion using the GSER [Eq. (5)] gives

$$G'_{true} = G'_{measured} - \frac{\kappa}{6\pi a}. \tag{9}$$

The trap stiffness can be calculated [41] from the corner frequency of the data taken in buffer at the same laser power, using $\kappa = 2\pi\gamma f_c$, where $\gamma = 6\pi\eta a$ is the Stokes drag on the bead. Horizontal lines of $G' = \kappa/(6\pi a)$, with κ derived from fitting Lorentzians to the PSDs, are plotted in Fig. 5 passing through the corresponding apparent $G'(f)$ curves, derived from the Kramers-Kronig integrals.

For fd concentrations below 0.2 mg/ml, the trap stiffness, even at low laser power, dominates the modulus such that with experimental noise, it becomes unreliable to extract the fd elastic modulus. At concentrations between 0.2 and 2 mg/ml, the trap dominates only at low frequencies, whereas the elastic modulus of the fd solution, which increases with frequency, dominates at the higher frequencies. Small bead-to-bead variations in κ, coming mainly from polydispersity in bead radius, cause large errors in the corrected elastic moduli at low frequencies when one uses the buffer experiments at the respective laser power to correct for the trap. Therefore, we used the average over the first few flat points of the uncorrected G' curves themselves to subtract from those curves to correct for the trap effect. An example of this trap correction in a 2 mg/ml fd solution is shown in Fig. 6. The 2 mg/ml fd PSD is shown in Fig. 6(a) (solid black line) with the buffer PSD at the same laser power (solid grey line) as a reference. The corresponding elastic modulus is shown in Fig. 6(b) (circles). The low-frequency part of the curve asymptotically approaches the apparent modulus due to the trap. Taking the average of the first six low-frequency points gives G'_{trap} (solid flat line). The fd elastic modulus (squares) is obtained by subtracting G'_{trap} from the total modulus.
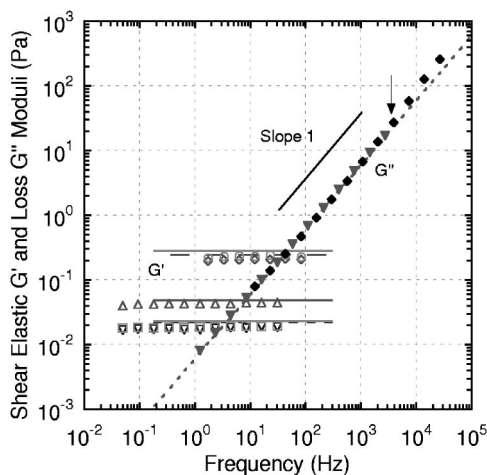

FIG. 5. $G'(f)$ (open symbols) of beads in buffer for five different laser powers. G'' data was averaged over three powers taken at a sampling rate of 20 kHz (filled inverted triangles) and averaged over two powers taken at a 195 kHz sampling rate (filled diamonds). Lines are $G' = \kappa/6\pi a$, where κ is the trap stiffness, and a is the radius of the bead. The straight line $G'' = 2\pi\eta f$ for the loss modulus in buffer passes through the G'' data points. The arrow indicates the frequency beyond which hydrodynamic effects become visible.
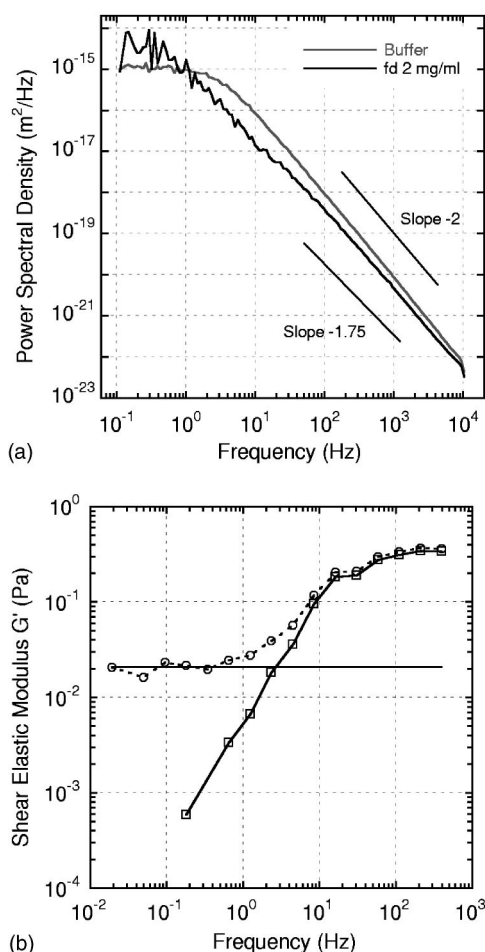
FIG. 6. (a) PSD for a bead in buffer (grey solid line) and a bead in 2 mg/ml fd solution (black solid line) at a fixed power. (b) $G'(f)$ before trap correction (circles), G' after trap correction (squares), and G' of the trap (flat line). The data are obtained from the 2 mg/ml fd PSD curve of (a).

For higher fd concentrations, between 5 and 14 mg/ml, the fd modulus dominates at all frequencies. We therefore use α_{true} of Eq. (8), with κ derived from fitting Lorentzians to the PSDs of buffer data at the same laser powers to obtain the corrected modulus G'_{true} for these concentrations. Bead polydispersity causes only a small error in these cases since the correction itself is relatively small to begin with.

E. Nonlinearity of the displacement detection and temperature effect

The interferometric displacement detection method is approximately linear for displacements up to about 200 nm (for 0.5 μm beads) from the center of the trap [45]. If the bead thermally moves to larger distances, the displacements are underreported. This would be expected to increasingly occur with decreasing laser power and with more compliant samples. In order to test if nonlinearity in the detection caused relevant errors in our experiments, we performed a measurement with a 0.5 μm diameter silica bead trapped in two superimposed laser foci of different colors— a 1064 nm

trap of varying power (14–140 mW) and a wider 830 nm trap of constant low power ($<$5 mW). The 1064 nm focus diameter is estimated [46] to be about 1.2 μm, and the 830 nm focus diameter was expanded to about four microns [46] by introducing a 1 mm pinhole in a plane conjugate to the back focal plane of the objective. A sketch of the setup is shown in Fig. 7(a). As the power in the 1064 nm focus is more and more reduced, the bead will thermally move to larger distances from the center of the trap. To the extent that the bead ventures beyond the linear region of the 1064 nm beam, the position data and so the PSD as measured by the narrow beam will be underreported. Figure 7(b) shows the PSDs measured by the 1064 nm beam at different power settings of the same trap using one and the same bead. Slight shifts in PSD curves are visible with curves corresponding to lower power settings lying below the ones corresponding to high powers, consistent with a slight nonlinearity effect in detection. This is a worst-case scenario. The linear regime of detection (it scales with bead size for large beads) is considerably higher for the larger 5 μm beads we use in our fd experiments. Furthermore, the fluctuations in the position of the larger beads will be lower in an elastic environment. Thus we conclude that the bead motion in our fd experiments was well within the linear range of detection. The effect of laser-induced heating, which would cause a qualitatively similar shift in the PSDs, was considered negligible for the following reasons: (i) As the power is increased, the solvent temperature increases (7.7 ± 1.2 K/W for water) [47], and its viscosity is reduced, which leads to larger fluctuations in the bead position and thus larger PSD values [47]. This temperature effect on the PSD in water solutions has been measured by Peterman, Gittes, and Schmidt [47] and was found to be $<$5% for a power range of 0–120 mW using a 1064 nm wavelength laser. (ii) Figure 7(c) shows the PSD of a 0.5 μm bead in buffer as measured by the wide 830 nm beam for different power settings of the narrow beam. No significant shift in the PSDs is measured, indicating that neither a temperature nor a nonlinear effect is detectable by the wide trap.

F. Controls for aggregation of fd around the probe bead

There are three possible effects that could cause the local concentration of fd in the vicinity of the probe bead to be different from the bulk fd concentration. (i) There might be direct attractive or repulsive interactions between the bead surface and the virus particles. (ii) There will in any case be an entropic steric interaction, causing a depletion zone in the absence of attractive interactions. (iii) There might be a dynamic pileup of virus due to the interaction with the laser trap. We controlled for direct attractive interactions of virus particles with silica beads by fluorescence microscopy and by atomic force microscopy (AFM). We fluorescently labeled virus particles with rhodamine and tracked the motion of single virus particles around trapped silica beads. In no cases did we see virus particles stuck to the beads. We then put a mixture of virus particles and beads on a glass slide and made AFM dry scans. We also did not observe any detectable increase in fd density around the beads in this test. We then controlled for a laser-induced dynamic pileup of the virus
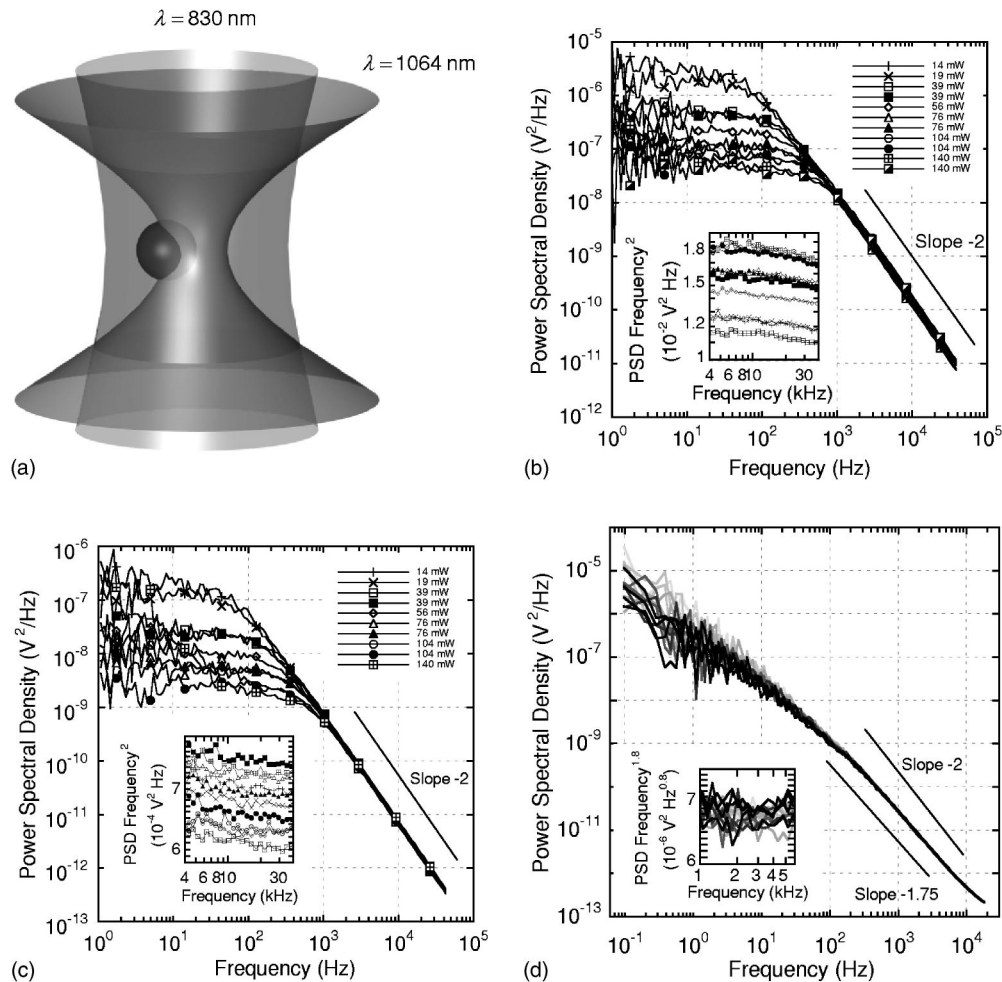
FIG. 7. (a) A sketch of the double laser trap setup used to test for the pileup of fd virus around a 0.5 μm diameter bead. The wide and narrow focused laser traps have wavelengths of 830 nm and 1064 nm, respectively. (b) PSD for a bead in buffer measured with the narrow 1064 nm wavelength laser trap for different power settings of the same trap (14–140 mW). Inset: PSD times the square of frequency for a portion of the high-frequency data. (c) PSD for a bead in buffer measured with the wide 830 nm wavelength laser trap for different power settings of the narrow trap (14–140 mW). Inset: PSD times the square of frequency for a portion of the high-frequency data. (d) PSD for the same sized bead in a concentrated 13.5 mg/ml fd solution measured with the wide trap for different power settings of the narrow trap (14–190 mW). Darker curves correspond to higher power settings of the narrow trap. Inset: PSD times the 1.8th power of frequency for a portion of the high-frequency data.

particles. We used the two colored beams sketched in Fig. 7(a) with beads in concentrated fd solution of 13.5 mg/ml. The wide 830 nm focus was of low power ($<$5 mW) and was used for displacement detection. The tight 1064 nm focus with variable laser power was used for trapping and was expected to pile up increasing amounts of fd around the bead with increasing trapping power. An increasing local fd concentration around the probe bead with increasing trapping power would shift the power spectra down at high frequencies due to increased viscosity, which lowers the position fluctuations of the bead. Figure 7(d) shows the PSD curves measured from one and the same trapped bead with the wide 830 nm beam for increasing power applied to the narrow beam. In the high-frequency part of the spectrum [Fig. 7(d) inset] we see no systematic shift in the PSD curves with power, excluding the possibility of any measurable buildup of virus particles around the bead. The low-frequency part of the spectra is different for different powers, reflecting the

increasing trap strength. The high-frequency tails of the PSD are curved slightly upward due to shot noise, since we used rather low power in the wide detection beam.

The depletion zone around a bead of radius a is expected to be of a thickness interpolating between bead radius and filament length or persistence length, as long as the latter two are larger than bead radius. If the bead is larger, then the shorter one of the two characteristic filament lengths will determine the depletion-layer thickness [11]. Filament and persistence length are about 1 μm. Therefore, we used beads of 5 μm diameter to reduce depletion effects. This works because even if the bead displacements are only nm, the Stokes flow field around the bead extends to a distance of about a around the bead and samples mostly undisturbed bulk medium in the case of 5 μm beads. The effects measured with smaller beads and a comparison of single-particle to dual-particle microrheology will be published elsewhere [48].
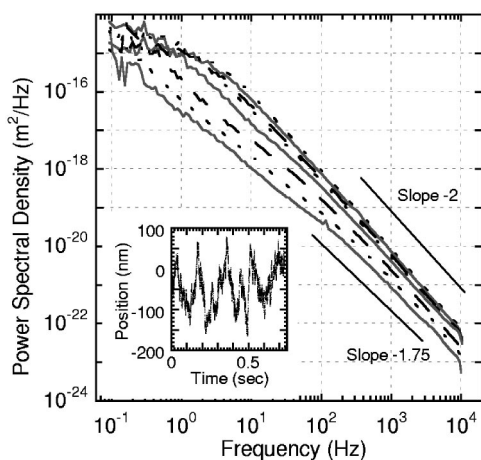
FIG. 8. PSD for beads in fd solutions of different concentration. Higher concentrations have lower PSD values. With this in mind, the curves for each fd concentration can be identified as follows: Buffer, 0.8, 11 mg/ml (dotted lines); 0.2, 2, and 14 mg/ml (solid lines); 0.4 and 5 mg/ml (dashed lines). Inset: A segment of the X position data for a bead in buffer, which corresponds to the buffer PSD curve.

IV. RESULTS AND DISCUSSION

A micrometer-sized bead optically trapped in a viscoelastic solution undergoes confined Brownian motion. For a purely viscous fluid the variance of the position fluctuations $x(t)$ is simply related via the equipartition theorem to the trap stiffness by [41] $\langle x(t)^2 \rangle = k_b T / \kappa$. The displacement variance is equal to the integral over the PSD. A change in viscosity alone will not change the variance and therefore the integral of the PSD, but will change its shape. It will still be a Lorentzian, but with a different corner frequency. A segment of the thermal fluctuations in the position of a bead trapped in buffer is shown in the inset of Fig. 8. The PSD curve corresponding to these fluctuations is the top dotted curve in Fig. 8. Adding a viscoelastic polymer to the solution will have two effects. The complex shear modulus G^* will generally increase and the PSDs will decrease in amplitude. Adding both a frequency-dependent loss and elastic modulus will also change the functional form of the PSDs, and they will no longer be Lorentzians. Figure 8 illustrates how the PSDs gradually change with increasing virus concentration. As expected PSD amplitudes decrease with increasing concentration. The slope of the curves at high frequencies deviates slightly from -2, below about 100 Hz this deviation is stronger, tending toward a slope of about -1.5 at the highest virus concentration. The corner frequency first moves to lower frequencies and then disappears entirely as the curves change shape.

In the following we will discuss the complex shear modulus of solutions of varying virus concentrations, derived from thermal fluctuation-time series data as described in Eqs. (3)–(5). Curves will only be presented after correction for the trap effects as described in Materials and Methods. Data were taken at several low powers at a sampling rate of 20 kHz and several high powers at a sampling rate of 195 kHz. Data are presented for both the elastic and loss

moduli after averaging over several beads and the two perpendicular spatial directions recorded for each power. Before averaging it was checked that X and Y fluctuations from each individual recording gave identical spectra within experimental noise. The elastic and loss moduli derived from the PSD data for the lowest, intermediate, and highest concentrations 0.2, 2, and 14 mg/ml are shown in Figs. 9(a), 9(b), and 9(c), respectively. G'' here includes both solvent and polymer contributions. At the concentration of 0.2 mg/ml [Fig. 9(a)], which is barely above the overlap concentration $c^*(0.04 \text{ mg/ml})$, the sample is predominantly viscous over the whole frequency range measured, with $G''(f)$ scaling as f^1 as expected for a (close to) Newtonian fluid. It should be noted that the elastic modulus $G'(f)$ has a very low absolute magnitude ($<10^{-2}$ Pa), which is very difficult to measure with macroscopic rheometers, but still reasonably well resolved in microrheology. With increasing fd concentration [Figs. 9(b) and 9(c)], both moduli increase and, relatively, the elastic character of the solution increases, with G' approaching G''. Even at 14 mg/ml, which is just below the isotropic-nematic phase transition, the elastic modulus is only on the order of 10 Pa, and the sample is still mainly viscous, i.e., it remains rather weakly entangled. This is due to the short contour length of the particles and to the charged surface of the fd virus, which prevents sticking between the particles. The increase in G' causes a shape change in the G'' curve and a decrease in (log-log) slope below 1 in the center part of the curves, in agreement with the Kramers-Kronig integral relationship between G' and G'' [Eqs. (3)–(5)]. In the terminal relaxation regime, which is best visible at the intermediate concentration, $G'(f)$ has a slope of 2, while $G''(f)$ has a slope of 1, as expected for rigid rods in fluid (see below). For the high-concentration sample the terminal relaxation regime moves to frequencies below the lower frequency limit of the instrument. At the high-frequency end of the curves, $G''(f)$ increases with approximate power-law behavior, the slope of which approaches 3/4 at high concentrations as predicted for semiflexible polymers (see below). $G'(f)$ is even for the highest concentration measured still in a transition regime between a plateaulike regime and the expected high-frequency scaling regime. In a true power-law regime G' and G'' must be parallel.

Figure 10 presents the full-concentration dependence of elastic and viscous moduli, respectively. The concentration dependence of $G'(f)$ is presented in Fig. 10(a). Virus concentrations ranged from 0.2 to 14 mg/ml, spanning the dilute to entangled regimes. $G'(f)$ shows a strong, more than 1000-fold increase in magnitude that reflects the increased degree of entanglement. The terminal relaxation regime is accordingly shifted to lower frequencies with increasing concentration, below the lower frequency limit of the experiment for the highest concentrations. A further indication of entanglement comes from a test of the scaling of the curves with concentration. In the dilute limit the elastic modulus has to scale linearly with concentration. In entangled solutions, at least at frequencies reflecting collective dynamic modes of the network, c-dependence will be stronger than linear. At high frequencies, when short-scale single-filament relaxations are dominating the response, both moduli will scale
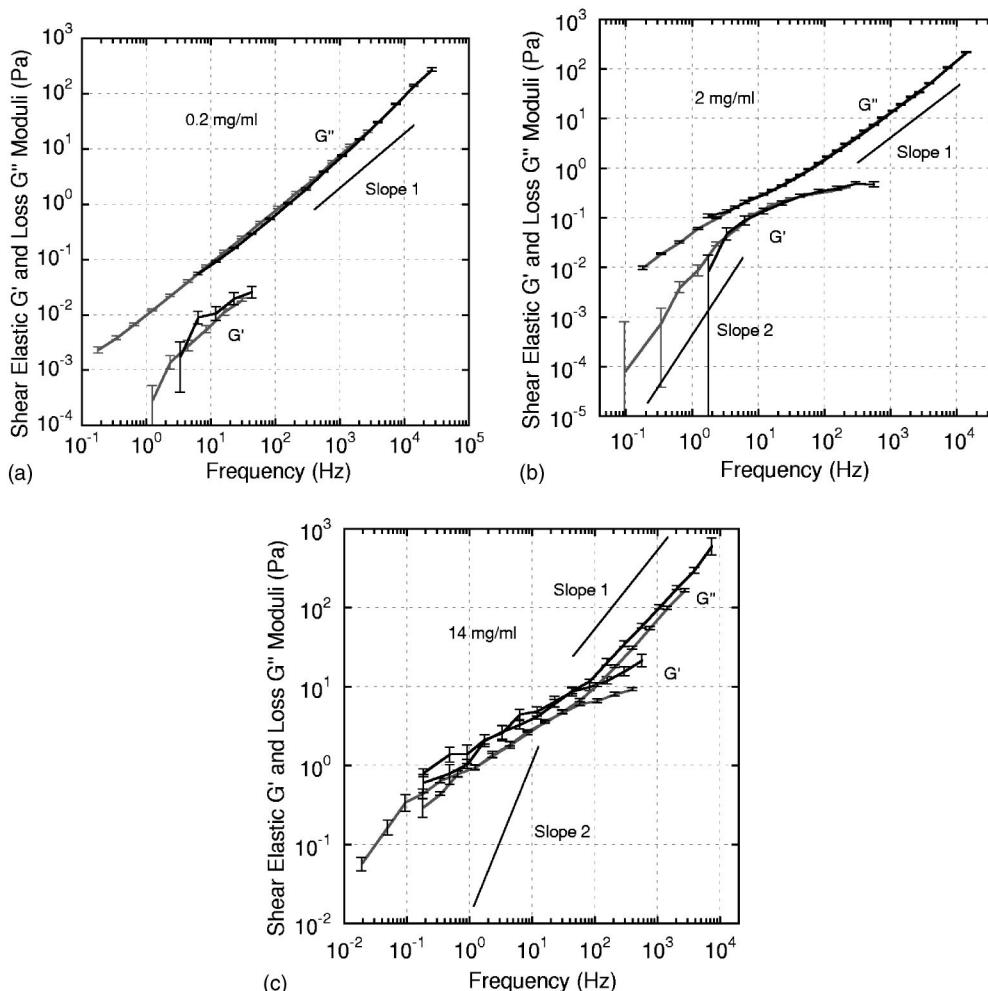
FIG. 9. (a) $G'(f)$ and $G''(f)$ for a 0.2 mg/ml fd solution. Low and high sampling rate data are distinguished by grey and black curves, respectively, for each modulus. (b) Similar data are presented for fd samples of concentration 2 mg/ml and (c) 14 mg/ml. Error bars indicate the standard deviation of the mean of the averaged data.

for all concentrations linearly with c again. Figure 10(b) shows $G'(f)$ divided by the respective fd concentrations. Curves for concentrations between 0.2 and 2 mg/ml overlap reasonably well within experimental error. This demonstrates that entanglement becomes relevant only at concentrations beyond 2 mg/ml, i.e., $c > 50\, c^*$. This result is consistent with other experiments on orientational dynamics of rod solutions, showing that the naive estimate of $c^* = 1/L^3$ seriously overestimates the dynamic consequences of steric rod-rod interactions [36,37]. The concentration dependence of the loss moduli for all concentrations is presented in Fig. 10(c). Circled points are buffer data and the straight line corresponds to the constant viscosity of water $G'' = 2\pi\eta f$. The loss modulus [Fig. 10(c)] changes with concentration also in a manner that demonstrates increasing entanglement, with the terminal relaxation regime moving to lower frequencies and with an intermediate plateaulike regime developing. The fact that G'' appears to extend beyond the collective-mode (or plateaulike) regime and approach the single-filament asymptotic slope of 3/4, whereas G' ends in the transition regime is mostly due to the fact that the finite high-frequency cutoff of the Kramers-Kronig integral strongly distorts G'

about a decade down from the cutoff—a part of the curves that is not plotted [11]. At frequencies above about 10 kHz, the low-concentration curves [see Fig. 10(c)], including the one in pure buffer, curve up, above the straight line corresponding to the loss modulus derived from water viscosity. The reason for that is the inertia of the solvent [see Sec. III C]. The concentration dependence of the loss moduli can also be visualized by plotting the viscosity [Fig. 10(d)], which is defined as $\eta(f) = G''(f)/2\pi f$. The buffer and polymer contributions to the stress tensor of the solution, and hence, the viscous modulus are additive [38]. The quantity that is measured experimentally is the total viscous modulus of both the buffer and polymer. In order to test the concentration scaling of the polymer G'', the solvent contribution has to be subtracted first. In Fig. 10(e), we plot $(G''(f) - G''_{buffer})$ divided by concentration. This plot demonstrates that all curves approximate a universal line curve at high frequencies, but deviate from this line at low frequencies in a concentration-dependent manner.

Figure 11 provides a comparison of our experimental results with published models. The lowest concentration sample for which we could reliably measure a storage modu-
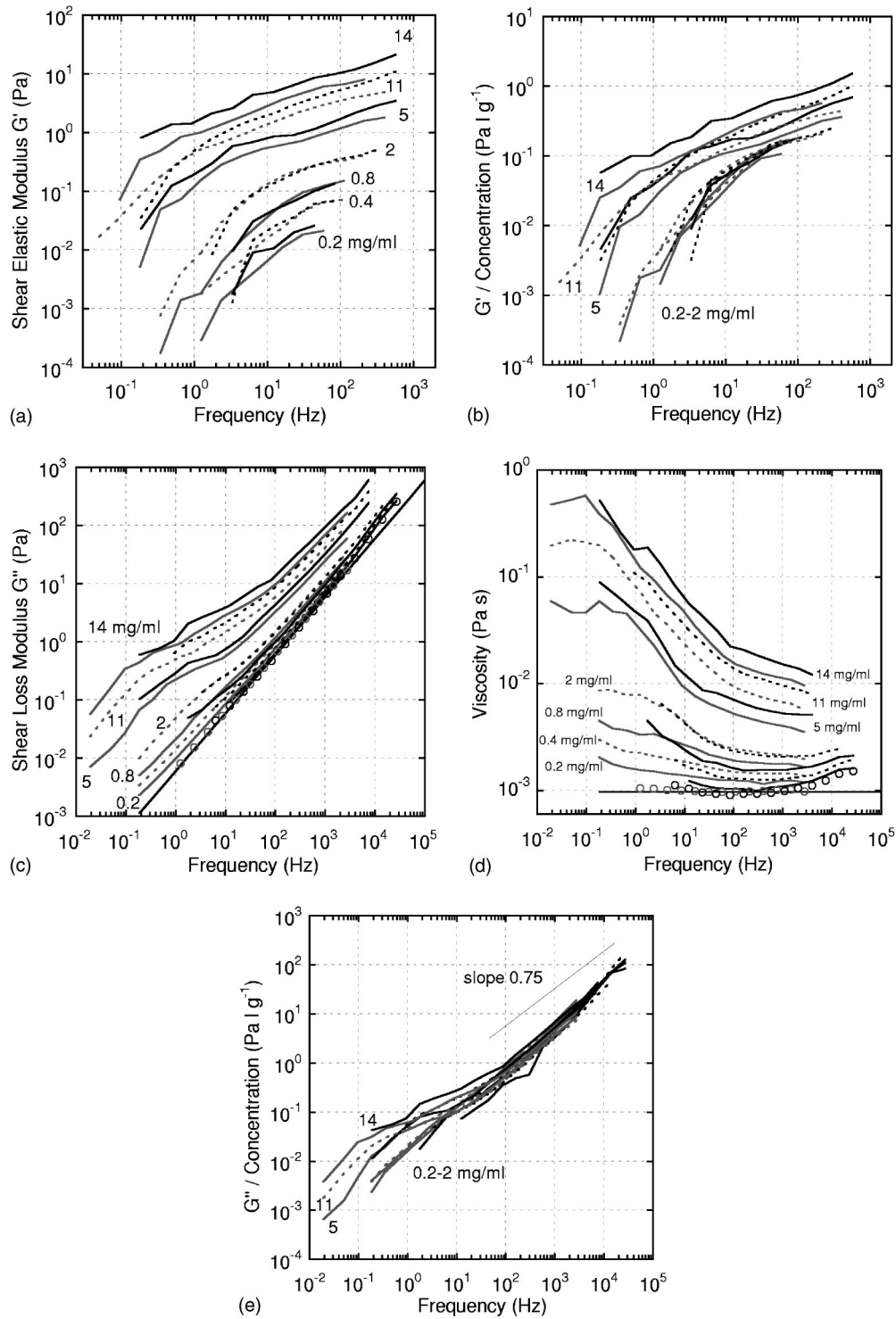
FIG. 10. (a) $G'(f)$ for beads in fd solutions of different concentration (indicated by numbers in mg/ml). Low and high sampling rate data are distinguished by grey and black colors respectively for each concentration. Pairs of curves for each concentration are plotted alternately in solid and dashed lines. (b) $G'(f)$ divided by concentration. (c) $G''(f)$ with buffer data (circles), and the theoretical loss modulus of buffer solution (solid black straight line). (d) The viscosity $\eta(f) = G''(f)/2\pi f$ and (e) $(G''(f) - G''_{buffer})$ divided by concentration.

lus was the 0.2 mg/ml solution. At this concentration, rather close to $c^*(0.04$ mg/ml), we expect to see mainly the moduli caused by the free rotation of unentangled rods. The moduli are expected to remain well described by the dilute theory predictions with the rotational diffusion coefficient replaced

by its reduced form of Eq. (10) as long as the concentration is not too high above c^*. At low frequencies where internal dynamic modes play no role, this behavior should be that of rigid rods, described by well-known models [38] [Eq. (11)]. At higher frequencies internal dynamic modes of the semi-
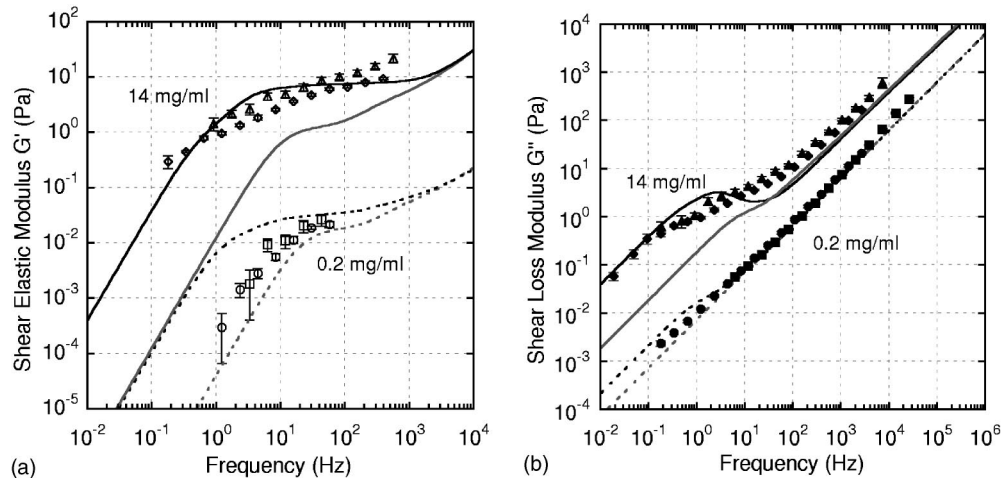
FIG. 11. (a) $G'(f)$ data for a 0.2 mg/ml fd solution taken at low and high sampling rates (open circles and squares, respectively), and for a 14 mg/ml fd solution taken at low and high sampling rates (open diamonds and triangles, respectively). Theory curves are shown for 0.2 mg/ml dilute (grey dashed line), tightly entangled (black dashed line), and for 14 mg/ml dilute (grey solid line), tightly entangled (black solid line). The same labeling scheme is used in (b) to plot $G''(f)$ using filled symbols for data points. Error bars indicate the standard deviation of the mean of the averaged data.

flexible rods will become apparent. A model that describes the dynamics of dilute solutions of semiflexible polymers is that of Shankar, Pasquali, and Morse [17], which is strictly valid in the limit of long filaments ($L \gg L_p$, see Appendix A, Sec. 2). Entanglements at higher concentrations will influence only the collective dynamics visible at the low-frequency end of the spectrum. We use the entangled theory of Morse [14,15] to compare to our high-concentration data. This theory is also strictly valid for long filaments ($L > L_e$). The storage modulus [Fig. 11(a)] measured for the dilute sample follows relatively closely the dilute rod limit. The slight shift of the data from the prediction of the dilute theory likely indicates that polymer hindrance is beginning to take place. The onset of the plateau occurs at $f_{rot} \sim 16$ Hz, corresponding to a rotational relaxation time τ_{rot} of about 10 ms. The dependence of the rotational diffusion coefficient on concentration at high ionic strength for fd virus has been studied using dielectric birefringence by Kramer *et al.* [37]. They reported a diffusion coefficient of $D_{ro} = 21.7 \pm 0.5$ s^{-1} below c^*. Up to a concentration of around $8c^*(0.32$ mg/ml), they have shown that the measured rotational diffusion values follow the relationship by Teraoka and Hayakawa [49] and Teraoka, Ookubo, and Hayakawa [50]

$$\frac{D_r}{D_{ro}} = \left(1 + \frac{\upsilon L^3}{\beta^{1/2}} \right)^{-2}, \tag{10}$$

where $\beta = 1.35 \times 10^3$ is a numerical factor and υ is the number of polymers per unit volume. Using Eq. (10), the rotational diffusion coefficient for the 0.2 mg/ml solution is predicted to be 17 s^{-1}. This corresponds to a rotational relaxation time $\tau_{rot} = 1/6D_r$ of 9.8 ms or a characteristic frequency of $f_{rot} = 1/(2\pi\tau_{rot}) = 16.2$ Hz. The expression for the dilute rigid-rod elastic modulus [38] is

$$G'(\omega) = \left(\frac{0.6 k_B T \upsilon \, \omega^2}{36 D_r^2 + \omega^2} \right), \tag{11}$$

where $\omega = 2\pi f$. To obtain a more quantitative comparison, we fit this expression to the 0.2 mg/ml G' data (Fig. 12) resulting in a rotational diffusion coefficient of 11.5 s^{-1}, in good agreement with the birefringence results. In Fig. 12 we plot the 0.2 mg/ml low sampling rate elastic modulus data with the dilute rigid-rod theory expression of Eq. (11) and the dilute semiflexible theory curve using the fitting parameter of 11.5 s^{-1} for the rotational diffusion coefficient for both theory curves. The arrow in Fig. 12 indicates the frequency $1/(2\pi\tau_{rot}) = 11$ Hz, below which the modulus is expected to relax by rotational diffusion (see Appendix, Sec. 2). Al-
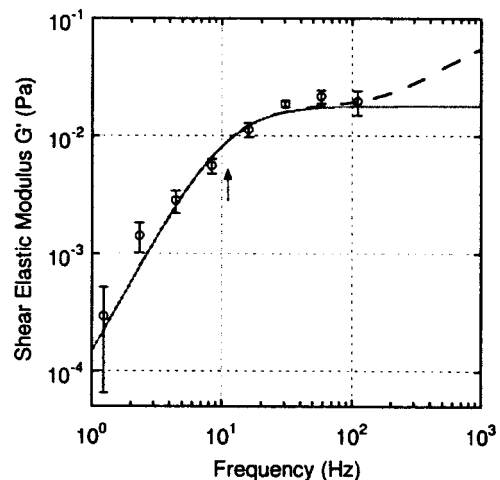

FIG. 12. $G'(f)$ of the 0.2 mg/ml low sampling rate data. The error bars indicate the standard deviation of the mean of the averaged data. The solid line is the dilute rigid rod theory G' curve. The dashed line is the dilute semiflexible theory G' curve. The arrow indicates the frequency $1/(2\pi\tau_{rot})$.

though the concentration is about five times higher than c^*, the results are clearly not well described by the entangled model plotted in Fig. 11(a) (see Appendix, Sec. 4). Figure 11(a) also compares G' for the most concentrated solution (14 mg/ml) with the two models. This concentration is far in the entangled regime and, consistent with that, the dilute model does not fit the data.

In the tightly entangled limit (see Appendix, Sec. 4), theoretical modeling is usually based on the concept of a tube in which each polymer exists [51] formed by intersecting filaments. It is often permissible to neglect the dynamics of the tube and only consider the motion of the polymer within a fixed tube because the relaxation of the tube is coupled to slow collective dynamics, whereas the motion of the entrapped chain is much faster single-chain dynamics. The entanglement length L_e is roughly the contour length between successive collisions of the polymer with the tube wall, depending on concentration and persistence length [Eq. (A2)]. The viscoelastic properties of the solution in the low frequency regime strongly depend on this length. For the tube model to be valid and particularly for the above-mentioned separation of time scales to apply, L must be much larger than L_e (this is a definition of the tightly entangled limit). There are two ways to obtain an estimate for the entanglement length. One method suggested by Morse [15,52] is to use F-actin data reported in the literature for the plateau modulus G' (see Appendix, Sec. 4). The other way is to use a different treatment of Morse [51] to calculate the tube diameter for tightly entangled semiflexible solutions and extract the entanglement length from the tube diameter (see Appendix, Sec. 4). The two methods lead to entanglement lengths that differ at most by 30% for concentrations higher than 5 mg/ml. Inspecting the ratio L_e/L shows that the 5, 8, 11, and 14 mg/ml fd solutions used in the experiments lie in the entangled regime, although the level of entanglement is weak, as the ratio remains on the order of unity. For the most concentrated solution of 14 mg/ml, the entangled model captures well the magnitude of the measured modulus [Fig. 11(a)]. The curve shape, however, is not well fitted. The limited applicability of the tube concept to our system and the difficulty in finding an exact method of obtaining the entanglement length makes the low-frequency, high-concentration theory prediction even less quantitatively reliable than the theory curves suggest in the figures.

The same comparison with theory is shown in Fig. 11(b) for the loss modulus G'' including the solvent contribution. Again for the low concentration of 0.2 mg/ml, the dilute rod limit is a reasonable fit, while at the highest concentration the magnitude of the modulus is well explained, the curve shape is again different. The crossover from low-frequency collective dynamics to high-frequency single-filament dynamics is expected to occur at a frequency larger than $1/(2\pi\tau_e)$ $=400$ Hz (see Appendix, Sec. 4). The loss modulus is seen to approach the predicted theory curve in Fig. 11(b) at frequencies above about 1 kHz, after strongly deviating in shape in the intermediate frequency range.

While G'' thus appears to approach a high-frequency power-law regime, G' clearly does not, and therefore the exact form of that power law cannot directly be read off the data. There is, however, a convenient method [53] to indi-rectly infer high-frequency dynamics from intermediate-frequency data by making two simple assumptions: (i) there is a (single-filament) scaling behavior at high frequencies where moduli scale linearly with concentration, independent of entanglement, and (ii) there is a plateau regime where the elastic modulus scales with a power larger than 1 with concentration due to entanglement. At high frequencies, the complex shear modulus of semiflexible polymer solutions is predicted to scale as $f^{3/4}$ and be dominated by single-filament tension dynamics [14–16]. The modulus will, therefore, be linear in concentration for such high frequencies. The G'' curves of Fig. 10(e) can be seen to approach this limit.

With the above assumptions the shear modulus can be written as [53]

$$G(f) = g_0 c^\alpha + g_1 c f^\beta, \quad (12)$$

where g_0 and g_1 are constants. In Fig. 13(a) we plot G' and $G'' - G''_{buffer}$ for all concentrations. We then (arbitrarily) choose one reference curve and find for each concentration c a factor $h(c)$ to multiply the modulus axis and a factor $j(c)$ to multiply the frequency axis, such that both the loss modulus at high frequencies and the elastic modulus in the plateau regime superimpose [Fig. 13(b)]. With these factors we can rewrite Eq. (12) to describe the universal curve, which should be, by construction, concentration independent:

$$h(c)G[f \cdot j(c)] = g_0 c^\alpha h(c) + g_1 c [f \cdot j(c)]^\beta h(c). \quad (13)$$

For the right-hand side to be concentration independent, $c^\alpha h(c)$ and $c \cdot j^\beta(c) \cdot h(c)$ have to be constants, i.e.,

$$\log[h(c)] = \text{const} - \alpha \log(c), \quad (14)$$

and

$$\log[c \cdot h(c)] = \text{const} - \beta \log[j(c)]. \quad (15)$$

Equations (14) and (15) are plotted in Figs. 13(c) and 13(d), respectively. From these curves we read off the plateau modulus concentration dependence of $\alpha=1.36$ (Pearson's $r=0.99$) and the high-frequency power-law exponent dependence of $\beta=0.63$ (Pearson's $r=0.98$). The power 1.36 is consistent with the predicted exponent of 7/5 (Morse) from the tube model. Thus even though the data show no well-developed plateau due to the short length of the filaments, the arguments leading to the scaling prediction in this collective dynamics regime appears to be valid. The high-frequency scaling is expected to be 3/4. This is only marginally consistent with our results. One reason for discrepancy might be that the transition between plateau and asymptotic power law may show additional structure. Morse predicts an intermediate regime caused by axial relaxation of tension through the free end of the filaments [15,17]. This is expected to change the power slope of G'' to closer to 1, steeper than we concluded from the scaling analysis. On the other hand, the broad transition from the collective (plateaulike) regime might have biased the result toward a smaller than the true power-law exponent.

V. CONCLUSIONS

We have applied a passive microrheology technique to extract the elastic and viscous shear moduli of solutions of
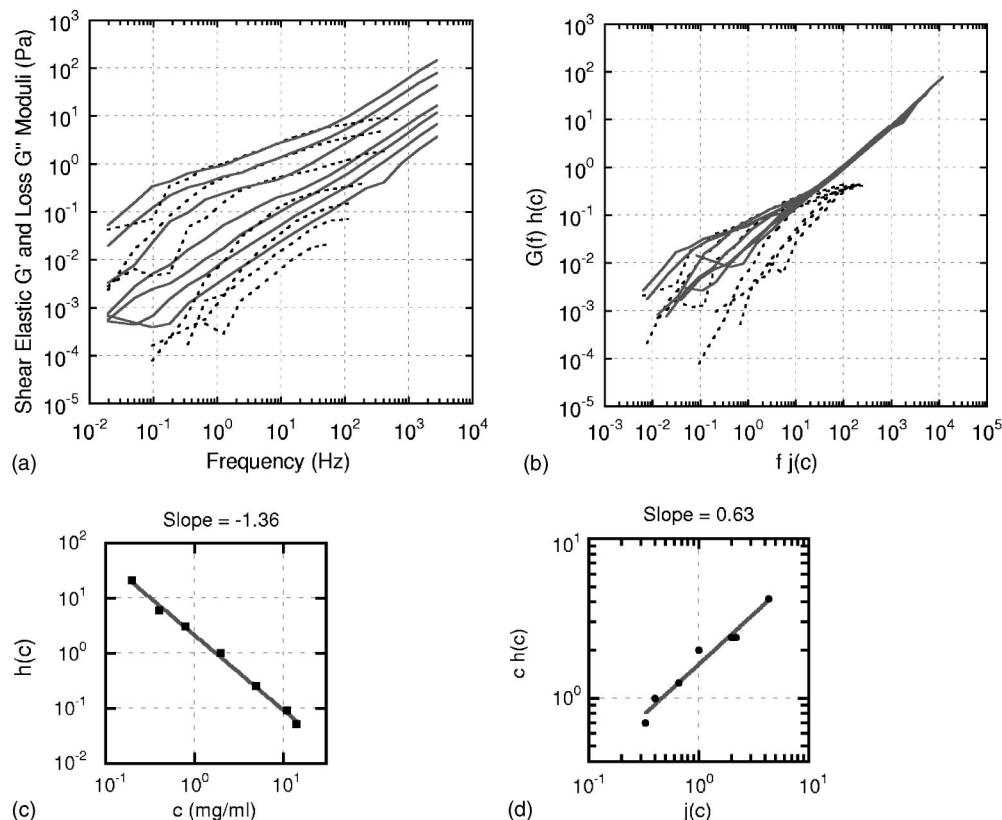
FIG. 13. (a) $G'(f)$ (dashed lines) and $G''(f) - G''_{buffer}$ (solid lines) of low sampling rate data for fd concentrations 0.2, 0.4, 0.8, 2, 5, 11, and 14 mg/ml. The curves follow the trend of higher modulus values for higher concentration solutions. (b) The result after scaling the frequencies and moduli in order for the $G''(f)$ curves to overlap at high frequency and the plateau height of G' to coincide. (c) Plot of the scaling parameter multiplying the moduli $h(c)$, as a function of concentration c, in mg/ml. (d) Plot of $h(c)$ times c as a function of the parameter multiplying the frequencies $j(c)$.

structurally well-characterized monodisperse semiflexible filamentous bacteriophage, covering more than six decades between 10^{-2} and 100 kHz. The concentrations of the solutions spanned the dilute, semidilute, and entangled regimes. Shear moduli were measured covering again about six decades in magnitude, from 10^{-3} to 1000 Pa. This demonstrates the unique capabilities of microrheology compared to conventional macroscopic methods. Where there are theoretical models, we found reasonable agreement, but there is presently no applicable model describing the collective entangled dynamics of short semiflexible polymers, leaving a challenge to the community.

APPENDIX

The appendix contains a sketch of the relevant theoretical treatments of semiflexible polymer systems in the dilute, semidilute, and tightly entangled limits and a discussion of the physical mechanisms and time dependence of the different contributions to the shear modulus of such systems.

1. Modulus

The theoretical approach of Morse [14,15] uses the Kramers-Kirkwood theory of viscoelasticity, which models a polymer as a primitive chain consisting of beads, which are point centers of hydrodynamic resistance in a solvent of viscosity η subjected to a macroscopic fluid velocity with a spatially homogeneous rate of deformation tensor. The stress tensor of such a solution has a contribution from the solvent and a contribution from the polymers inside the solvent. Forces between different polymers are seen to be negligible and only intramolecular contributions within a polymer are considered. Once the total or partial stress tensor is derived, the corresponding dynamic modulus $G(t)$ is obtained by looking at the relaxation of stress when the system is subjected to a step strain at zero time. The complex modulus $G(f) = G'(f) + iG''(f)$ is then the Fourier transform of the dynamic modulus where G' and G'' are the elastic and viscous

moduli, respectively. The expression for the shear modulus of a solution of semiflexible polymers has the general form

$$G = G_{solvent} + G_{curve} + G_{orient} + G_{tens}, \qquad (A1)$$

where the curvature term arises from both bending forces and the orientational entropy of the links. The orientational term is a residual contribution of the orientational entropy arising from the two end links of the primitive chain. The tension term arises from the constraint forces that resist extension of the links of the chain. An outline of the different approaches of treating dilute, semidilute, and tightly entangled solutions is presented below along with the time dependence and the physical origin of the relevant time scales of the dynamic modulus for each concentration regime.

2. Dilute theory

The approach outlined below for the dilute theory of semiflexible polymers is that of Shankar, Pasquali, and Morse [17]. The approach is based on solving a Langevin equation, which describes the Brownian motion of a single free-draining wormlike chain in an imposed mean flow. The equation relates the hydrodynamic frictional forces acting on the chain with the bending energy force and the constraint (tension) force that enforces inextensibility of the chain. Theoretical curves presented in our paper correspond to an analytical approximation of the full theory.

Time scales

(i) The shortest time scale is that required for strain and tension to diffuse the entire length of the chain $\tau_{\parallel} \sim L^8/L_p^5$. The modulus for times much shorter than $\tau_{\parallel}$ is expected to decay as $t^{-3/4}$. (ii) The next relaxation time corresponds to the longest wavelength bending mode of a semiflexible rod of length L, $\tau_{\perp} \sim L^4/L_p$. For times $\tau_{\parallel} < t < \tau_{\perp}$, the modulus is expected to decay as $t^{-5/4}$. (iii) The longest relaxation time is due to the rotational diffusion of the rods in the solution $\tau_{rod} \sim L^3$. This relaxation time is the terminal relaxation time of flow-induced anisotropies in the distribution of rod orientations. The modulus for times much longer than τ_{rod} is expected to decay as $e^{-t/\tau_{rod}}$, as for rigid rods.

The time scales form a hierarchy $\tau_{\parallel} < \tau_{\perp} < \tau_{rod}$ and become more separated as the semiflexible rods approach the rigid-rod limit, i.e., as L/L_p decreases. For the fd system where $L/L_p \approx 1/2$ the intermediate time regime will shrink leading to a featureless crossover from $t^{-3/4}$ to exponential rod diffusion decay.

The curves for the dilute semiflexible theory of Figs. 11(a), 11(b), and 12 are obtained from the analytical approximation (Eqs. 141 of Ref. [17]) of the full theory (Eqs. 124 of Ref. [17]). The input parameters to the model for fd solutions are the diameter of the filament $d=7$ nm, contour length $L=0.9$ μm, persistence length $L_p=2.2$ μm, concentration of the solution c, solution temperature, $T=21.4\,°C$, and the solvent viscosity $\eta=0.969 \times 10^{-3}$ N·s/m².

3. Semidilute theory

As the solution concentration is increased above the dilute limit, polymers start to hinder each other leading to a reduc-

tion in the rotational diffusion coefficient, but fluctuations in the bending modes of the polymers are unaffected. As the concentration approaches the tightly entangled limit, both the orientation and shape of polymers are affected by the presence of other polymers. A tube picture for the polymers starts to develop. However, the form of the moduli in this regime has not been worked out analytically.

4. Tightly entangled theory

Recent theoretical treatment by Morse [14,15] describes the viscoelastic behavior of tightly entangled solutions of semiflexible polymers. This concentration regime is characterized by the following: (i) polymers exist on short time scales within a tube of diameter $D_e \ll L_p$, (ii) motions along the tube contour are resisted by the viscous drag due to the solvent, (iii) the shape of the tube deforms affinely in response to macroscopic deformation of the solution, and (iv) excluded-volume interactions between polymers are neglected except for keeping the polymer in its tube.

The entanglement length L_e is a phenomenological parameter in the order of the contour length between points on the filament where collisions with the walls of the tube occur. The onset of the tightly entangled regime is roughly estimated to occur when the contour length equals the entanglement length.

Time scales

(i) The time scale $\tau_{\parallel}$ required for tension to diffuse the length of the chain has the same form as the dilute case. (ii) The relaxation time τ_e, of a bending mode of wavelength equal to the entanglement length L_e of the polymer in its tube is the relevant time scale that corresponds to $\tau_{\perp}$ in the dilute case. It has the same form as $\tau_{\perp}$ with the contour length replaced by the entanglement length. The modulus at time scales below τ_e has a $t^{-3/4}$ dependence. This modulus is from the single-filament dynamics contribution, i.e., it is proportional to concentration. It does not depend on the degree of entanglement of the polymer in the network, and it has the same form in dilute and entangled solutions. (iii) For the entangled case, a polymer exists in a tube and diffuses along its contour length, a process that is called reptation. The relaxation time associated with this diffusion is of the order of time needed for the polymer to diffuse its own contour length $\tau_{rep} \sim L^3$. (iv) The longest time scale, which corresponds to its dilute counterpart τ_{rod}, has the length dependence $\tau_{rod} \sim L^2 L_p$, but it is much larger than the dilute case since in a concentrated solution, the polymer is much more constrained and must diffuse many times its own length before its orientation changes.

For $f \lesssim (2\pi\tau_e)^{-1}$, the decay of stress is seen to be mainly the result of diffusion due to reptation for curvature and orientation stress terms, whereas for $f \gtrsim (2\pi\tau_e)^{-1}$, the modulus is expected to be dominated by the tension component.

The curves for the entangled semiflexible theory plotted in Figs. 11(a) and 11(b) are obtained from a numerical evaluation of Eqs. 124 of Ref. [15]. The input parameters to the model for fd solutions are the diameter of the filament $d=7$ nm, contour length $L=0.9$ μm, persistence length L_p

$=2.2$ μm, concentration of the solution c, solution temperature $T=21.4\,°$C, solvent viscosity $\eta=0.969\times10^{-3}$ $N\cdot$s/m^2, and the entanglement length L_e.

One method to obtain the entanglement length suggested by Morse [52] is to use known data of F-actin solutions to estimate this parameter. There is an undetermined prefactor in the equation relating the entanglement length to the persistence length and contour length density [14]

$$L_e=b\rho^{-2/5}L_p^{1/5}. \tag{A2}$$

The prefactor b is assumed to be a universal parameter independent of the kind of polymer system under study. Sackmann and coworkers reported values for the storage plateau modulus $G'_{plateau}\sim1-2$ dyne/cm^2 for F-actin solutions at a concentration of 1 mg/ml. The Morse theory [15] gives the following expression for the plateau modulus assuming it is dominated by a curvature stress contribution

$$G'_{curve}=\frac{7}{5}\frac{\rho\,T}{L_e}. \tag{A3}$$

In order to obtain a plateau modulus of 1 dyne/cm^2, which is comparable to the experimental result, and using values for the persistence length $L_p=17$ μm, contour length density $\rho=39$ μm^{-2}, and temperature $T=295$ K, the value for the en-

tanglement length of actin solution is found to be $L_e=2.2$ μm, and so the prefactor b is estimated to be 5.4. Equation (A2) is then applied to fd, with a persistence length $L_p=2.2$ μm and the contour length density $\rho=\{[fd](\text{mg/ml})L(\text{cm})\}/m_p(\text{mg})$, where m_p is the polymer mass of fd, to obtain the concentration dependence of the entanglement length.

The relation between the entanglement length and tube diameter was derived by Odijk [54] $L_e\sim D_e^{2/3}L_p^{1/3}$. The other way to determine the entanglement length is to use a model, for estimating the tube diameter, and relate it to the entanglement length. Such a model has been proposed for tightly entangled semiflexible solutions [51]. Two different mechanisms are provided that give different power-law dependence on concentration and persistence length. One gives a detailed description of the interaction of a polymer with single nearby polymers, but neglects the collective elastic relaxation of the network. This approach yields $L_e^{BCA}=3.45\rho^{-2/5}L_p^{1/5}$ (Eq. 47 in Ref. [51]). The other approach treats the surrounding network around a polymer as an elastic continuum with shear modulus equal to the self-consistently determined plateau modulus of the solution and gives $L_e^{EMA}=1.70\rho^{-1/3}L_p^{1/3}$ (Eqs. 9 and 65 in Ref. [51]). We use a combination of both approaches that was suggested by Morse [52] $L_e=((L_e^{BCA})^4+(L_e^{EMA})^4)^{1/4}$.

[1] T. D. Pollard, Nature (London) **422**, 741 (2003).
[2] S. Y. Bershitsky *et al.*, Nature (London) **388**, 186 (1997).
[3] G. Bao and S. Suresh, Nat. Mater. **2**, 715 (2003).
[4] P. G. De Gennes, J. Chem. Phys. **55**, 572 (1971).
[5] M. Doi and S. F. Edwards, J. Chem. Soc., Faraday Trans. 2 **74**, 1789 (1978); **74**, 1802 (1978); **74**, 1818 (1978).
[6] M. Doi and S. F. Edwards, J. Chem. Soc., Faraday Trans. 2 **75**, 38 (1979).
[7] M. Doi, J. Phys. (Paris) **36**, 607 (1975).
[8] M. Doi and S. F. Edwards, J. Chem. Soc., Faraday Trans. 2 **74**, 568 (1978); **74**, 918 (1978).
[9] T. Gisler and D. A. Weitz, Phys. Rev. Lett. **82**, 1606 (1999).
[10] T. G. Mason *et al.*, J. Rheol. **44**, 917 (2000).
[11] B. Schnurr, F. Gittes, F. C. MacKintosh, and C. F. Schmidt, Macromolecules **30**, 7781 (1997).
[12] D. T. Chen *et al.*, Phys. Rev. Lett. **90**, 108301 (2003).
[13] M. L. Gardel *et al.*, Phys. Rev. Lett. **91**, 158302 (2003).
[14] D. C. Morse, Macromolecules **31**, 7030 (1998).
[15] D. C. Morse, Macromolecules **31**, 7044 (1998).
[16] F. Gittes and F. C. MacKintosh, Phys. Rev. E **58**, R1241 (1998).
[17] V. Shankar, M. Pasquali, and D. C. Morse, J. Rheol. **46**, 1111 (2002).
[18] H. Isambert and A. C. Maggs, Macromolecules **29**, 1036 (1995).
[19] R. Everaers, F. Jülicher, A. Ajdari, and A. C. Maggs, Phys. Rev. Lett. **82**, 3717 (1999).
[20] A. C. Maggs, Phys. Rev. E **55**, 7396 (1996).
[21] R. G. Larson, *The Structure and Rheology of Complex Fluids* (Oxford University Press, Oxford, 1998).

[22] F. C. MacKintosh and C. F. Schmidt, Curr. Opin. Colloid Interface Sci. **4**, 300 (1999).
[23] T. G. Mason *et al.*, Phys. Rev. Lett. **79**, 3282 (1997).
[24] A. W. C. Lau *et al.*, Phys. Rev. Lett. **91**, 198101 (2003).
[25] F. G. Schmidt, B. Hinner, E. Sackmann, and J. X. Tang, Phys. Rev. E **62**, 5509 (2000).
[26] A. J. Levine and T. C. Lubensky, Phys. Rev. E **63**, 041510 (2001).
[27] E. J. G. Peterman, M. A. v. Dijk, L. C. Kapitein, and C. F. Schmidt, Rev. Sci. Instrum. **74**, 3246 (2003).
[28] L. A. Day and R. L. Wiseman, *The Single-Stranded DNA-Phages* (Cold Spring Harbor Laboratory, New York, 1978).
[29] L. Makowski, *The Structures of Biological Macromolecules and Assemblies* (Wiley, New York, 1984), Vol 1.
[30] S. Bhattacharjee, M. J. Glucksmann, and L. Makowski, Biophys. J. **61**, 725 (1992).
[31] L. A. Day, C. J. Marzec, S. A. Reisberg, and A. Casadevall, Annu. Rev. Biophys. Biophys. Chem. **17**, 509 (1988).
[32] E. Loh, Biopolymers **18**, 2569 (1979).
[33] E. Loh, E. Ralston, and V. N. Schumaker, Biopolymers **18**, 2549 (1979).
[34] T. Maeda and S. Fujime, Macromolecules **18**, 2430 (1985).
[35] K. Zimmermann *et al.*, J. Biol. Chem. **261**, 1653 (1986).
[36] C. Graf *et al.*, J. Chem. Phys. **98**, 4920 (1993).
[37] H. Kramer *et al.*, Macromolecules **25**, 4325 (1992).
[38] M. Doi and S. Edwards, *The Theory of Polymer Dynamics* (Oxford University Press, New York, 1986).
[39] J. Sambrook, E. F. Fritsch, and T. Maniatis, *Molecular Cloning: A Laboratory Manual* (Cold Spring Harbor, New York, 1989).

[40] M. W. Allersma *et al.*, Biophys. J. **74**, 1074 (1998).

[41] F. Gittes and C. F. Schmidt, Methods Cell Biol. **55**, 129 (1998).

[42] F. Gittes (unpublished).

[43] K. Berg-Sorensen and H. Flyvbjerg (unpublished).

[44] A. J. Levine (unpublished).

[45] F. Gittes and C. F. Schmidt, Opt. Lett. **23**, 7 (1998).

[46] A. E. Siegman, *Lasers* (University Science Books, Mill Valley, CA, 1986).

[47] E. J. G. Peterman, F. Gittes, and C. F. Schmidt, Biophys. J. **84**, 1308 (2003).

[48] K. Addas, J. X. Tang, and C. F. Schmidt (unpublished).

[49] I. Teraoka and R. Hayakawa, J. Chem. Phys. **91**, 2643 (1989).

[50] I. Teraoka, N. Ookubo, and R. Hayakawa, Phys. Rev. Lett. **55**, 2712 (1985).

[51] D. C. Morse, Phys. Rev. E **63**, 031502 (2001).

[52] D. C. Morse (private communication).

[53] F. C. Mackintosh and D. A. Weitz (private communication).

[54] T. Odijk, Macromolecules **16**, 1340 (1983).